

# Enhanced Optical Measurement and Stress Quantification of Film Roll Wrinkling in Roll-to-Roll Processing

Shih-Chen Shi<sup>\*</sup>, Hung-Wei Rao<sup>\*</sup> and Dieter Rahmadiawan<sup>\*,\*\*</sup>

**Keywords** : Stress quantification; Roll-to-roll processing; Soft film; Film wrinkling; Optical measurement

## ABSTRACT

Roll-to-roll (R2R) processing is a widely used continuous manufacturing technique for flexible materials. However, the formation of longitudinal ridges, known as "tin-canning," remains a challenge, leading to uneven coating thickness, surface defects, and increased production costs. Currently, there are limited methods for real-time quantification of tin-canning during production. This study introduces an optical measurement system to quantify film wrinkling through image processing. A chessboard calibration corrects lens distortion, and a mathematical model reconstructs the cross-sectional profile of wrinkles. The system achieves an amplitude error of less than 9% and a wavelength error of less than 2%. Additionally, the critical tensile stress at ridges is determined using buckling stress formulas and finite element modeling (FEM). The results provide insights into film ridging mechanisms and stress distributions, enhancing quality control in R2R manufacturing.

## INTRODUCTION

Roll-to-roll (R2R) technology is an advanced and efficient manufacturing process used for fabricating flexible electronic devices, thin films, and coatings. It continuously processes components on a flexible substrate, significantly streamlining the traditional sheet-to-sheet process by reducing the number of steps from seven to three (Czyzewski et al., 2020; Nguyen et al., 2015; Xie et al., 2018). Regarding

energy consumption, the R2R process employs additive manufacturing techniques, allowing material utilization rates to exceed 95%, reducing overall production costs by more than 30%, and cutting carbon emissions by over 50%. Additionally, R2R technology is widely applied in the fabrication of solar cells (Angmo et al., 2013; Dou et al., 2018; Espinosa et al., 2011; Hwang et al., 2015; Krebs, 2009a, 2009b; Krebs et al., 2009; Krebs et al., 2010; Søndergaard et al., 2012). However, a common issue observed post-R2R processing is the appearance of longitudinal ridges on the surface of the rolled material, known as "tin-canning" (Hommes & Keegan Jr, 1991; Walker & Cole, 2015). This phenomenon can lead to uneven film coating thickness and affect the product's appearance, potentially necessitating a re-rolling process that consumes time and significantly increases production costs.

Plastic films, made from continuous polymeric materials, are pervasively used in various applications, including packaging, construction, and industrial processes (Gasni et al., 2024; Rahmadiawan et al., 2024; Shi, Hsieh, et al., 2024). Commonly used materials include polyethylene, polypropylene, and polyester (Ammala et al., 2011; Baumgarten, 1992; Ferrer-Balas et al., 2001; Shi, Lu, et al., 2024). Due to their low bending stiffness, these films can undergo tensile deformations along the direction of tension when the applied tension exceeds the stiffness of the material, accompanied by lateral contractions. These lateral contractions introduce compressive stresses, leading to buckling and the formation of wrinkled deformations (Jin et al., 2015; Shi, Cheng, et al., 2024; Wang et al., 2022; Wang et al., 2016).

The human visual system utilizes binocular disparity to perceive the three-dimensional shape of objects by imaging the same object from different angles with each eye and then processing these images through the visual nervous system to compute and form stereoscopic vision (Muryy et al., 2013; Prazdny, 1987; Qian, 1997). Previous studies have experimented with displaying vertical and horizontal striped images on two LCD monitors to enable machines to recognize three-dimensional objects similarly. After being

*Paper Received March, 2025. Revised May, 2025. Accepted June, 2025. Author for Correspondence: Shih-Chen Shi.*

<sup>\*</sup> Department of Mechanical Engineering, National Cheng Kung University, 70101 Tainan, Taiwan

<sup>\*\*</sup> Department of Mechanical Engineering, Universitas Negeri Padang, 25173 Padang, Sumatera Barat, Indonesia

reflected off a surface, images captured by a CCD camera were calculated using geometrical optics principles to measure the contours of discontinuous surfaces on the measurement platform and store the data numerically (Bothe et al., 2004; Zhang et al., 2012; Zhang et al., 2021). Other research involved using two CCD cameras and an LCD to capture images of striped patterns reflected from surfaces. These images were then used to calculate and reconstruct the three-dimensional contours of the reflective surfaces (Balzer & Werling, 2010; Perard & Beyerer, 1997; Xu et al., 2020). Both methods successfully demonstrated how binocular disparity, combined with image processing and principles of geometrical optics, can be utilized to achieve the optical measurement of object contours.

Lens distortion refers to the perspective distortions that arise when capturing images through optical lenses, typically consisting of multiple lens elements. Light passing through these elements results in imaging flaws, particularly noticeable as distortion at the image edges. This defect includes "barrel distortion," where the image expands outward, and "pincushion distortion," where it contracts inward (Ricolfe-Viala & Sanchez-Salmeron, 2010; Shah & Aggarwal, 1994). To correct these distortions, previous research involved capturing images of a chessboard at various angles using a digital camera and identifying the corners of the chessboard squares using Hough transforms (Czyzewski et al., 2020; Nguyen et al., 2015; Xie et al., 2018). This method allows for the identification of the direction of image distortion. By spatially realigning the corners of the squares, the image can be adjusted to display the chessboard in an undistorted state. The parameters obtained from this adjustment process are then used as correction parameters for the camera and lens to correct the distortion in captured images (Bennett & Lasenby, 2014; De la Escalera & Armingol, 2010; Douskos et al., 2007).

According to the relevant literature and reference books on material mechanics (Bedford & Liechti, 2019; Boreis & Schmidt, 2002; Craig Jr & Taleff, 2020; Muvdi & McNabb, 2012; Ugural & Fenster, 2011), the strain tensor for Hooke's law can be represented as shown in Equation (1-3).

$$\varepsilon_x = \frac{1}{E}(\sigma_x - \nu\sigma_y - \nu\sigma_z) \quad (1)$$

$$\varepsilon_y = \frac{1}{E}(-\nu\sigma_x + \sigma_y - \nu\sigma_z) \quad (2)$$

$$\varepsilon_z = \frac{1}{E}(-\nu\sigma_x - \nu\sigma_y + \sigma_z) \quad (3)$$

Here,  $E$  denotes the modulus of elasticity, and  $\nu$  represents Poisson's ratio. Given that the values for normal stress and normal strain in thin plates are exceedingly small, they can be considered negligible, leading to  $\sigma_z = 0$  and  $\varepsilon_z = 0$  (Bauchau & Craig, 2009;

Bloom & Coffin, 2000; Kubiak, 2013). Furthermore, due to the significant difference in dimension between the length and thickness of the plate, experiments have shown that transverse line elements remain straight at the center of the plate, thereby suppressing anticlastic curvature. At the center of the plate, the transverse normal stress  $\sigma_y$  is non-zero; however, the transverse normal stress disappears at the free edges of the plate. Consequently, anticlastic curvature only forms in a narrow region near the free edges to accommodate the disappearance of the normal stress there. In the center of the plate, the associated normal strain is zero, and the suppression of anticlastic curvature is characterized by the absence of the normal strain  $\varepsilon_y = 0$ . This value is then substituted into the formula for critical compressive stress at buckling, ultimately deriving the critical buckling pressure formula for thin plate materials, as shown in Equation (4) (Kubiak, 2013).

$$\sigma_{cr} = \pi^2 \frac{E}{12(1-\nu^2)} \left(\frac{t}{a}\right)^2 \quad (4)$$

This study hypothesizes that horizontal lines marked on the film surface will form specific curves due to ridge distortion. Surface morphology is captured through photography, followed by lens distortion correction to eliminate edge warping. Data extraction and curve fitting techniques reconstruct the curves in a 2D coordinate system. The fitted curves are then compared with the actual cross-sectional profile for correction, establishing the measurement model. This workflow aligns with recent educational research emphasizing the importance of computational thinking and algorithmic visualization in engineering disciplines (Sakti et al., 2024). The second hypothesis is that the critical buckling stress formula for thin flat plates can be applied to film materials. This formula calculates the tensile stress at each ridge, which is then input into finite element analysis to simulate the ridge deformation amplitude under the calculated stress. The simulated amplitudes are compared with measured values to validate the tensile stress calculations.

## MATERIALS AND EXPERIMENT

### Materials

The materials used in this study are polymethyl methacrylate (CHANG MING, Taiwan), Carbon Steel Flange Fixing Seat (XIN YI, Taiwan), Hardened Stainless Steel Rod (XIN YI, Taiwan), Polyethylene Terephthalate (Univacco, Taiwan), Acrylic Paint (Univacco, Taiwan), and Aluminum (Univacco, Taiwan).

### Film Molds Preparation

Different waveform molds with varying wavelengths and amplitudes were designed using SOLIDWORKS, and engineering drawings were generated. The

dimensions and part numbers of each mold are listed in Table 1. The molds were made from 6 mm thick acrylic sheets, cut using a CO<sub>2</sub> laser cutting machine with a precision of 0.3 mm. A sample mold is shown in Fig. 1(a). The molds were assembled using aluminum rods and flanges. Polyethylene terephthalate (PET) film was cut into 5 cm × 10 cm rectangles, and straight lines were drawn parallel to the long edge of the film using a permanent marker. The films were then adhered to the curved edges of the molds with glue, as shown in Fig. 1(b).

Table 1. List of waveform molds used in the experiments.

Sample	Wavelength (mm)	Amplitude (mm)	Length (mm)
1	15	6	10
2	15	5	10
3	15	4	10
4	5	3	10

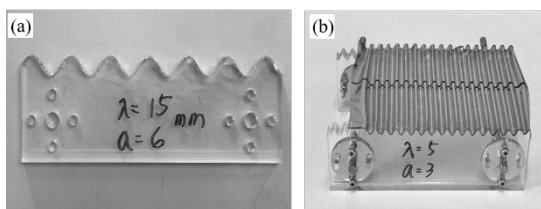


Fig. 1 (a) Sample of the film corrugation mold (b) Completed sample of the film corrugation mold.

### Imaging Film Corrugation with Known Dimension

The completed film mold was positioned upright on a horizontal surface. A Canon EOS 100D digital camera equipped with a Canon EF-S 18-55mm f/3.5-5.6 IS STM lens was used for image capture. The camera was placed 25 cm away from the film surface, with the lens axis parallel to the surface. The focal length was set to 18 mm, aperture to f/8, and the camera was tilted at an angle of 20°. The tripod height was adjusted to align the marked lines at the center of the frame. Fig. 2(a) shows a schematic of the camera setup, and Fig. 2(b) shows the actual setup.

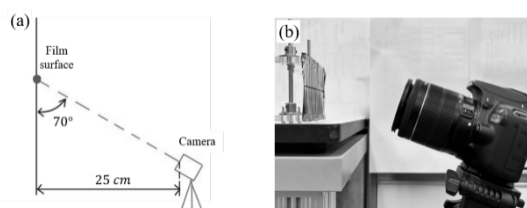


Fig. 2 Schematic layout (a), and actual setup of the experimental camera used during the measurements.

### Applying lens distortion correction

A standard chessboard was created and photographed using a Canon EOS 100D camera with an EF-S 18-55mm f/3.5-5.6 IS STM lens. The photography parameters are listed in Table 2. The images were imported into MATLAB, where the detectCheckerboardPoints function was used to detect the chessboard pattern and assign coordinates to the grid intersection points. The rotmat2vec3d and translationVector functions were applied to sort the pixel coordinates, aligning them horizontally and vertically. The worldToImage function was then used to adjust the pixel positions according to the corrected coordinates, restoring the undistorted image of the chessboard. The calibration parameters were saved as a .mat file and applied to subsequent images to eliminate lens distortion.

Table 2. Photography Parameters

Focal Length (mm)	Shutter Speed (s)	Aperture	ISO
18	1/125	f/11	6400

### Extraction of Data Points From The Images And Curve Fitting Performance

The captured image was cropped to 750 × 375 pixels and imported into MATLAB using the Grabit function. A Cartesian coordinate system was established with the lower-left corner as the origin (0,0), the lower-right corner as (50,0), and the upper-left corner as (0,50). Data points were marked along the curve in the image, and their coordinates were stored in an n×2 matrix and then exported as a MAT file. Curve fitting was performed to construct a linear function that best fits the data points, using linear regression to determine the optimal function parameters. In this study, MATLAB's Curve Fitter tool applied the Sum of Sines and non-parametric modeling techniques for linear regression analysis, fitting the extracted data points to generate the curve profile.

### Establish a Mathematical Transformation Model

The measurement steps were performed on a film corrugation mold with a wavelength of 15 mm and an amplitude of 6 mm. Using MATLAB, a sine function curve was plotted on a 2D coordinate system to represent the groove cross-section. The fitted function curve was compared with the actual profile, and the measured data points were scaled horizontally and vertically to approximate the cross-section. These adjustments were used to develop a mathematical transformation model, which was applied to measure other film corrugation molds for validation.

### Calculation of Critical Buckling Stress for The

**Film**

The film corrugation cross-sectional dimensions obtained from the previous experiments were analyzed by treating each corrugation peak as a half-wave of a sine function. The wavelength and amplitude values were then substituted into the curve length formula to calculate the total length of the curve.

$$S = \int_{x_1}^{x_2} \sqrt{1 + (f'(x))^2} dx \tag{5}$$

Let  $x_1$  and  $x_2$  be two adjacent points where the sine function intersects the x-axis, and  $f'(x)$  represents the first derivative of the sine function with the same amplitude and wavelength as the groove. This calculates the original flat plate length before buckling at each corrugation peak. After obtaining the original length of the film groove, the material is treated as a rectangular thin plate. The critical buckling pressure formula for thin plates, Eq. (4), is applied to calculate the buckling stress in the lateral compression direction at each groove. The relationship between stress and strain is then expressed using the Generalized Hooke's Law.

$$\epsilon_x = \frac{1}{E}(\sigma_x - \nu(\sigma_y + \sigma_z)) \tag{6}$$

$$\epsilon_y = \frac{1}{E}(\sigma_y - \nu(\sigma_x + \sigma_z)) \tag{7}$$

$\epsilon_x$  and  $\epsilon_y$  are the strains in two directions, and  $\nu$  is the Poisson ratio.  $\sigma_x$ ,  $\sigma_y$ , and  $\sigma_z$  represent the stresses in the three directions. Since the stress in the direction perpendicular to the thin plate is negligible, we assume  $\sigma_z=0$ . Thus, the two equations can be simplified as follows.

$$E\epsilon_x = \sigma_x - \nu\sigma_y \tag{8}$$

$$E\epsilon_y = \sigma_y - \nu\sigma_x \tag{9}$$

By dividing and simplifying the two equations, we obtain Eq. (10).

$$\sigma_y = \frac{2\nu}{1+\nu^2} \sigma_x \tag{10}$$

The lateral compressive stress calculated from Eq. (4) is substituted into Eq. (10) to determine the tensile stress at the groove in the stretching direction.

**Finite Element Modeling and Analysis Using Abaqus**

After calculating the tensile stress at each groove using the thin-plate critical buckling stress formula, Abaqus software was used to simulate the deformation of the film material under tensile stress, including the resulting groove morphology and dimensions. The calculated tensile stress was applied to the film model to simulate the groove formation, and the simulated groove amplitude was compared with the measured amplitude to validate the tensile stress calculations.

**RESULTS AND DISCUSSION**

**Model Mathematical Scale Acquisition**

A thin-film wrinkle model with a wavelength of 15 mm and an amplitude of 6 mm is used as the reference for establishing the mathematical model. Fig. 3 (a) shows the image of the marked lines captured by the imaging device. However, the captured image exhibits distortion due to lens distortion caused by optical refraction. To address this, a checkerboard calibration method was applied to correct the distortion, and Fig. 4 (b) presents the image after calibration and cropping to a resolution of  $750 \times 375$  pixels.

Once the image was calibrated and cropped, the MATLAB Gribit function was used to open the image and define key reference points: the origin, the maximum x-axis position, and the maximum y-axis position. Data points were then marked along the curve's shape. After completing this process, the curve was extracted as two-dimensional numerical data, as shown in Fig. 3 (c). Next, MATLAB Curve Fitter was employed to fit the curve using the Sum of Sine function, selecting the curve with the smallest root mean square error (RMSE). Fig. 3 (d) shows the fitted curve, and Fig. 3 (e) compares the fitted and actual curves. Finally, the two-dimensional data was adjusted by scaling the horizontal and vertical directions to ensure that the wavelength and amplitude errors between the fitted and actual curves were less than 5%. The error calculations are summarized in Table 3, and the scaling factors were applied to develop the mathematical model.

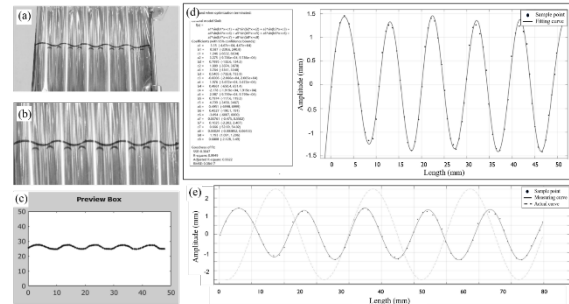


Fig. 3 (a) Image of the marked lines captured by the imaging device. (b) Image after calibration and cropping to a resolution of  $750 \times 375$  pixels. (c) The extraction of the curve from the image into two-dimensional numerical data. (e) The comparison between the fitted curve and the actual curve.

Table 3. The error calculation results of the mathematical model for measuring the groove with a wavelength of 15 mm and an amplitude of 6 mm.

**Detailed Measurement Results of a Single Waveform Groove Profile**

After establishing the mathematical model, the measurement system was validated by first measuring a thin-film wrinkle curve model formed by a single sine function. Two sets of thin-film wrinkle molds, both with a wavelength of 15 mm and amplitudes of 5 mm and 4 mm, were measured. Each measurement recorded the "amplitude" and "wavelength" and compared them to the actual curve to calculate the error. Each mold was measured three times to obtain the average error. Fig. 4 (a) shows the cross-sectional profile of the 15 mm wavelength, 5 mm amplitude mold, with the error results detailed in Table 4. The average amplitude error is approximately 5.07%, and the average wavelength error is about 1.11%, corresponding to an amplitude error of 0.25 mm and a wavelength error of 0.17 mm. Next, the cross-sectional profile for the 15 mm wavelength, 4 mm amplitude mold is shown in Fig. 4 (b), with error calculations in Table 5. The results show an average amplitude error of 3.67% and an average wavelength error of 0.49%, corresponding to an amplitude error of 0.25 mm and a wavelength error of 0.20 mm.

To further assess the system's accuracy for molds with smaller wavelengths and amplitudes, a thin-film wrinkle mold with a wavelength of 5 mm and an amplitude of 3 mm was created. The cross-sectional profile is shown in Fig. 4 (c), and the error calculations are listed in Table 6. The average amplitude error was approximately 8.67%, and the average wavelength error was 0.60%, with amplitude and wavelength errors of 0.25 mm and 0.03 mm, respectively.

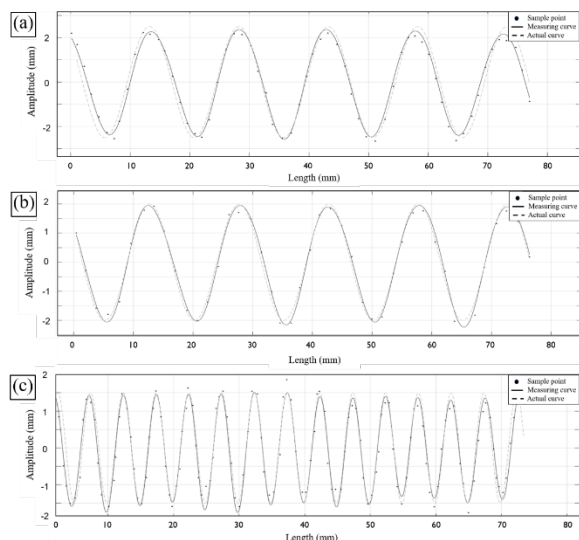


Fig. 4. Cross-sectional profile measurement results of the thin-film wrinkle mold with a wavelength of 15 mm and an amplitude of 5 mm (a), a wavelength of 15 mm and an amplitude of 4 mm (b), and a wavelength of 5 mm and an amplitude of 3 mm (c).

Count	Average Amplitude Error (mm)	Average Wavelength Error (mm)	Amplitude Error (%)	Error (%)
1	0.28	0.18	4.67	1.20
2	0.19	0.07	3.17	0.47
3	0.30	0.34	5.00	2.27
Average	0.26	0.20	4.28	1.31

Table 4. Error calculation results of the mathematical model for measuring the groove with a wavelength of 15 mm and an amplitude of 5 mm.

Count	Average Amplitude Error (mm)	Average Wavelength Error (mm)	Amplitude Error (%)	Error (%)
1	0.27	0.01	5.40	0.07
2	0.28	0.22	5.60	1.47
3	0.21	0.27	4.20	1.80
Average	0.25	0.17	5.07	1.11

Table 5. Error calculation results of the mathematical model for measuring the groove with a wavelength of 15 mm and an amplitude of 4 mm.

Count	Average Amplitude Error (mm)	Average Wavelength Error (mm)	Amplitude Error (%)	Error (%)
1	0.18	0.09	4.50	0.60
2	0.15	0.08	3.75	0.53
3	0.11	0.05	2.75	0.33
Average	0.15	0.07	3.67	0.49

Table 6. Error calculation results of the mathematical model for measuring the groove with a wavelength of 15 mm and an amplitude of 3 mm.

Count	Average Amplitude Error (mm)	Average Wavelength Error (mm)	Amplitude Error (%)	Error (%)
1	0.21	0.02	7.00	0.40
2	0.17	0.01	5.67	0.20
3	0.40	0.06	13.33	1.20
Average	0.26	0.03	8.67	0.60

### Measurement Results of Superimposed Waveform Grooves

After completing the measurements on the thin-film groove mold based on a single sine function, the experiment proceeded to create a mold that more closely resembles the actual conditions of thin-film grooves. To achieve this, a thin-film mold was designed using a superposition of two sine functions, with wavelengths of 7 mm and 10 mm, and amplitudes of 2 mm for both. The curve equation is given by eq. (11).

$$f(x) = \sin\left(\frac{2\pi}{7}x\right) + \sin\left(\frac{2\pi}{10}x\right) \quad (11)$$

Table 7 presents the error calculation results for measuring this model using the system, while Fig. 5 shows the cross-sectional profile measurement results. The average measurement error is 0.66 mm.

Table 7. Error calculation results of the mathematical model for measuring the superimposed waveform grooves.

Count	Average Amplitude Error (mm)
1	0.64
2	0.65
3	0.68
Average	0.66

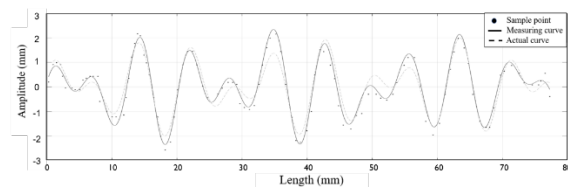


Fig. 5. Cross-sectional profile measurement results of the superimposed waveform grooves based on the mathematical model.

### Measurement Results of Surface Wrinkles On The Thin-Film Roll

To validate the measurement system's performance on real thin-film rolls used in production lines, a PET film roll with an outer diameter of 234 mm and a width of 139 mm was selected as the measurement target. The same measurement method was applied, and the results are shown in Fig. 6. The experimental results showed that the measurement system can accurately detect surface wrinkles with an amplitude greater than 0.4 mm on the thin-film roll. In comparison, wrinkles with an amplitude less than 0.4 mm are adjusted to 0 mm.

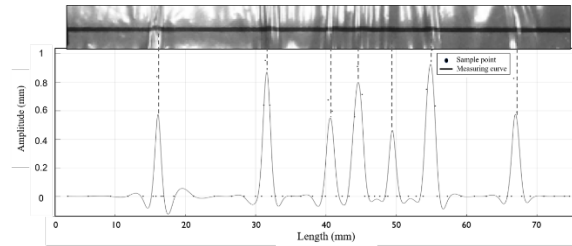


Fig. 6. Comparison between the measured surface wrinkles on the thin film roll and the actual captured images.

### Tensile Stress In The Thin-Film Roll Grooves Calculation

After experimentally obtaining the cross-sectional profile of the thin-film wrinkles, the MATLAB findpeaks function was used to identify the coordinates of the peaks, numbered as shown in Fig. 7. The same approach was applied to determine the coordinates of the troughs. The y-coordinate of each peak was used as the amplitude, and the difference between the x-coordinates of the neighboring troughs on either side of the peak was calculated as the half-wavelength. These values were then substituted into Eq. (5) to compute the original length of the wrinkle before buckling deformation. This length was treated as the flat plate length, and the material properties of PET from Table 8 were used for calculations. The critical buckling stress at each wrinkle (peak) was determined, and this value was used to calculate the local tensile stress. The results of these calculations are shown in Table 9.

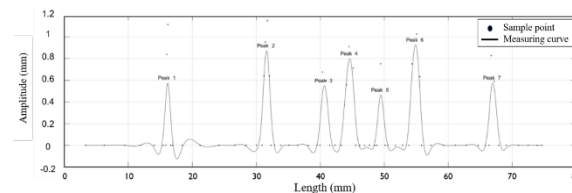


Fig. 7. Results of Peak Position Identification

Table 8. Material Properties of PET.

Thickness (m)	Poisson ratio	Young's modulus (GPa)
$12 \times 10^{-6}$	0.337	10.4

Table 9. Critical Buckling Stress and Critical Tensile Stress at Each Groove (Peak).

Peak Stress (Pa)	1	2	3	4	5
The critical buckling stress	138820	81152	92510	75928	132671
The critical buckling tension	229356	134078	152843	125447	219196

**Finite Element Method Simulation Results**

To validate the tensile stress calculation results for the thin film, roll grooves obtained in the previous section, this experiment utilized the finite element method (FEM) using Abaqus software. The experimentally calculated tensile stress was applied to the thin-film material, and the deformation of the material under this stress was simulated. The simulated groove amplitudes were then compared with the measured groove amplitudes. Fig. 8 shows the tensile simulation results for each thin-film groove, and Table 10 compares the simulated and measured groove amplitudes. The average amplitude difference between the two was 0.021 mm, with an average percentage difference of 3.26%. These simulation results confirm the tensile stress calculated for the grooves in the previous experiment.

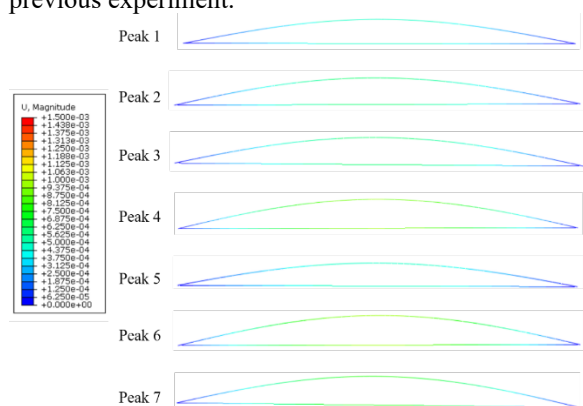


Fig. 8. Tensile Deformation Diagram of the Thin-Film Model.

Table 10. Comparison Between Simulated and Measured Groove Amplitudes.

Peak	1	2	3	4	5
Tensile stress (Pa)	229356	134078	152843	125447	219196
Measured amplitude (mm)	0.575	0.873	0.551	0.800	0.464
Simulated amplitude (mm)	0.562	0.813	0.562	0.813	0.438
Amplitude difference (mm)	0.013	0.060	0.011	0.012	0.026
Difference percentage (%)	2.36%	7.39%	2.01%	1.53%	6.04%

**CONCLUSION**

This study addresses the measurement and quantification of groove formation in roll-to-roll processes, specifically during the winding of film rolls. The objective is to achieve this through optical measurement and image processing techniques. It is hypothesized that horizontal lines marked on the film surface will form characteristic curves due to groove

distortion. By capturing the surface profile of the film, the experimental results demonstrate that the measurement model achieves an amplitude error of less than 9% and a wavelength error of less than 2% for the groove molds. Additionally, this system can detect grooves with amplitudes of 0.4 mm or greater on the film surface, thereby reconstructing the film’s cross-sectional profile. In the next phase, the film material is modeled as a thin plate, and the critical buckling stress formula for thin plates is used to calculate the tensile stress at each groove in the wound film. The experimental results successfully calculated the tensile stress at each groove based on its cross-sectional dimensions. This tensile stress was then applied to the film material in Abaqus software, using the finite element method (FEM) to simulate the deformation caused by the stress. The simulated groove amplitudes differed from the measured values by an average of 0.021 mm, with a percentage difference of 3.26%, validating the tensile stress calculations.

This study provides a method for measuring and analyzing groove formation caused by uneven surface tension in films. It has potential applications in process monitoring and quality control in roll-to-roll manufacturing and contributes to a deeper understanding of the relationship between film tension and groove formation mechanisms.

**Acknowledgements**

This work was supported by the National Science and Technology Council, Taiwan (grant numbers 112-2221-E-006-173, 113-2221-E-006-087-MY2, 113-2221-E-006-112-MY2, and 113-2221-E-006-116). We gratefully acknowledge the Core Facility Center of National Cheng Kung University for allowing us to use their EM000700 equipment. We also acknowledge the partial support of the Higher Education Sprout Project, Ministry of Education to the Headquarters of University Advancement at National Cheng Kung University (NCKU).

**References**

Ammala, A., Bateman, S., Dean, K., Petinakis, E., Sangwan, P., Wong, S., Yuan, Q., Yu, L., Patrick, C., & Leong, K. (2011). An overview of degradable and biodegradable polyolefins. *Progress in Polymer Science*, 36(8), 1015-1049.

Angmo, D., Larsen-Olsen, T. T., Jørgensen, M., Søndergaard, R. R., & Krebs, F. C. (2013). Roll-to-roll inkjet printing and photonic sintering of electrodes for ITO free polymer solar cell modules and facile product integration. *Advanced Energy Materials*, 3(2), 172-175.

Balzer, J., & Werling, S. (2010). Principles of shape from specular reflection. *Measurement*, 43(10),

- 1305-1317.
- Bauchau, O. A., & Craig, J. I. (2009). *Structural analysis: with applications to aerospace structures* (Vol. 163). Springer Science & Business Media.
- Baumgarten, W. W. (1992). Apparatus comprising an extruder and a calender for producing sheets and/or foils from plastic or rubber mixtures. In: Google Patents.
- Bedford, A., & Liechti, K. M. (2019). *Mechanics of materials*. Springer Nature.
- Bennett, S., & Lasenby, J. (2014). ChESS–Quick and robust detection of chess-board features. *Computer Vision and Image Understanding*, 118, 197-210.
- Bloom, F., & Coffin, D. (2000). *Handbook of thin plate buckling and postbuckling*. CRC Press.
- Boresi, A. P., & Schmidt, R. J. (2002). *Advanced mechanics of materials*. John Wiley & Sons.
- Bothe, T., Li, W., von Kopylow, C., & Juptner, W. P. (2004). High-resolution 3D shape measurement on specular surfaces by fringe reflection. *Optical Metrology in Production Engineering*.
- Craig Jr, R. R., & Taleff, E. M. (2020). *Mechanics of materials*. John Wiley & Sons.
- Czyzewski, M. A., Laskowski, A., & Wasik, S. (2020). Chessboard and chess piece recognition with the support of neural networks. *Foundations of Computing and Decision Sciences*, 45(4), 257-280.
- De la Escalera, A., & Armingol, J. M. (2010). Automatic chessboard detection for intrinsic and extrinsic camera parameter calibration. *Sensors*, 10(3), 2027-2044.
- Dou, B., Whitaker, J. B., Bruening, K., Moore, D. T., Wheeler, L. M., Ryter, J., Breslin, N. J., Berry, J. J., Garner, S. M., & Barnes, F. S. (2018). Roll-to-roll printing of perovskite solar cells. *ACS Energy Letters*, 3(10), 2558-2565.
- Douskos, V., Kalisperakis, I., & Karras, G. (2007). Automatic calibration of digital cameras using planar chess-board patterns. *Proceedings of the 8th Conference on Optical*,
- Espinosa, N., Garcia-Valverde, R., Urbina, A., & Krebs, F. C. (2011). A life cycle analysis of polymer solar cell modules prepared using roll-to-roll methods under ambient conditions. *Solar Energy Materials and Solar Cells*, 95(5), 1293-1302.
- Ferrer-Balas, D., MasPOCH, M. L., Martinez, A., & Santana, O. (2001). Influence of annealing on the microstructural, tensile and fracture properties of polypropylene films. *Polymer*, 42(4), 1697-1705.
- Gasni, D., Rahmadiawan, D., Irwansyah, R., & Khalid, A. E. (2024). Composite of Carboxymethyl Cellulose/MXene and Span 60 as Additives to Enhance Tribological Properties of Bio-Lubricants. *Lubricants*, 12(3), 78.
- Hommel, W. J., & Keegan Jr, J. J. (1991). Apparatus for drawing plastic film in a tenter frame. In: Google Patents.
- Hwang, K., Jung, Y. S., Heo, Y. J., Scholes, F. H., Watkins, S. E., Subbiah, J., Jones, D. J., Kim, D. Y., & Vak, D. (2015). Toward large scale roll-to-roll production of fully printed perovskite solar cells. *Advanced materials*, 27(7), 1241-1247.
- Jin, L., Takei, A., & Hutchinson, J. W. (2015). Mechanics of wrinkle/ridge transitions in thin film/substrate systems. *Journal of the Mechanics and Physics of Solids*, 81, 22-40.
- Krebs, F. C. (2009a). Polymer solar cell modules prepared using roll-to-roll methods: Knife-over-edge coating, slot-die coating and screen printing. *Solar Energy Materials and Solar Cells*, 93(4), 465-475.
- Krebs, F. C. (2009b). Roll-to-roll fabrication of monolithic large-area polymer solar cells free from indium-tin-oxide. *Solar Energy Materials and Solar Cells*, 93(9), 1636-1641.
- Krebs, F. C., Gevorgyan, S. A., & Alstrup, J. (2009). A roll-to-roll process to flexible polymer solar cells: model studies, manufacture and operational stability studies. *Journal of Materials Chemistry*, 19(30), 5442-5451.
- Krebs, F. C., Tromholt, T., & Jørgensen, M. (2010). Upscaling of polymer solar cell fabrication using full roll-to-roll processing. *Nanoscale*, 2(6), 873-886.
- Kubiak, T. (2013). *Static and dynamic buckling of thin-walled plate structures*. Springer.
- Muryy, A. A., Welchman, A. E., Blake, A., & Fleming, R. W. (2013). Specular reflections and the estimation of shape from binocular disparity. *Proceedings of the National Academy of Sciences*, 110(6), 2413-2418.
- Muvdi, B. B., & McNabb, J. (2012). *Engineering mechanics of materials*. Springer Science & Business Media.
- Nguyen, T., Vo, Q. N., Kim, Y., & Lee, G. (2015). Tensor voting, hough transform and SVM integrated in chess playing robot. *Proceedings of the 9th International Conference on Ubiquitous Information Management and Communication*,
- Perard, D., & Beyerer, J. (1997). Three-dimensional measurement of specular free-form surfaces with a structured-lighting reflection technique. *Three-Dimensional Imaging and Laser-Based Systems for Metrology and Inspection III*,
- Prazdny, K. (1987). Detection of binocular disparities. In *Readings in Computer Vision* (pp. 73-79). Elsevier.
- Qian, N. (1997). Binocular disparity and the perception of depth. *Neuron*, 18(3), 359-368.
- Rahmadiawan, D., Abral, H., Azka, M. A., Sapuan, S.

- M., Admi, R. I., Shi, S.-C., Zainul, R., Azril, Zikri, A., & Mahardika, M. (2024). Enhanced properties of TEMPO-oxidized bacterial cellulose films via eco-friendly non-pressurized hot water vapor treatment for sustainable and smart food packaging [10.1039/D4RA06099G]. *RSC Advances*, 14(40), 29624-29635.
- Ricolfe-Viala, C., & Sanchez-Salmeron, A.-J. (2010). Lens distortion models evaluation. *Applied optics*, 49(30), 5914-5928.
- Sakti, R. H., Jalinus, N., Sukardi, S., Hidayat, H., Wulansari, R. E., Tin, C. T., & Ayasrah, F. T. M. (2024). Diving into the Future: Unravelling the Impact of Flowgorithm and Discord Fusion on Algorithm and Programming Courses and Fostering Computational Thinking. *International Journal of Learning, Teaching and Educational Research*, 23(7), 347-367.
- Shah, S., & Aggarwal, J. (1994). A simple calibration procedure for fish-eye (high distortion) lens camera. Proceedings of the 1994 IEEE international Conference on Robotics and Automation,
- Shi, S.-C., Cheng, S.-T., & Rahmadiawan, D. (2024). Developing biomimetic PVA/PAA hydrogels with cellulose nanocrystals inspired by tree frog structures for superior wearable sensor functionality. *Sensors and Actuators A: Physical*, 379, 115981.
- Shi, S.-C., Hsieh, C.-F., & Rahmadiawan, D. (2024). Enhancing mechanical properties of polylactic acid through the incorporation of cellulose nanocrystals for engineering plastic applications. *Teknomekanik*, 7(1), 20-28.
- Shi, S.-C., Lu, F.-I., Wang, C.-Y., Chen, Y.-T., Tee, K.-W., Lin, R.-C., Tsai, H.-L., & Rahmadiawan, D. (2024). Rice straw-derived chitosan-enhanced plasticizers as biologically and environmentally friendly alternatives for sustainable materials. *International Journal of Biological Macromolecules*, 264, 130547.
- Søndergaard, R., Hösel, M., Angmo, D., Larsen-Olsen, T. T., & Krebs, F. C. (2012). Roll-to-roll fabrication of polymer solar cells. *Materials today*, 15(1-2), 36-49.
- Ugural, A. C., & Fenster, S. K. (2011). *Advanced mechanics of materials and applied elasticity*. Pearson Education.
- Walker, T. J., & Cole, K. (2015). Tin-canning defects in thin film winding.
- Wang, T., Yang, Y., & Xu, F. (2022). Mechanics of tension-induced film wrinkling and restabilization: a review. *Proceedings of the Royal Society A*, 478(2263), 20220149.
- Wang, Y., Li, Z., & Xiao, J. (2016). Stretchable thin film materials: fabrication, application, and mechanics. *Journal of Electronic Packaging*, 138(2), 020801.
- Xie, Y., Tang, G., & Hoff, W. (2018). Geometry-based populated chessboard recognition. Tenth International Conference on Machine Vision (ICMV 2017),
- Xu, F., Zhang, Y., & Zhang, L. (2020). An effective framework for 3D shape measurement of specular surface based on the dichromatic reflection model. *Optics Communications*, 475, 126210.
- Zhang, H., Ji, L., Liu, S., Li, S., Han, S., & Zhang, X. (2012). Three-dimensional shape measurement of a highly reflected, specular surface with structured light method. *Applied optics*, 51(31), 7724-7732.
- Zhang, Z., Chang, C., Liu, X., Li, Z., Shi, Y., Gao, N., & Meng, Z. (2021). Phase measuring deflectometry for obtaining 3D shape of specular surface: a review of the state-of-the-art. *Optical Engineering*, 60(2), 020903-020903.